

# Impact of Dynamical Fermions on QCD Vacuum Structure

Peter J. Moran and Derek B. Leinweber  
*Special Research Centre for the Subatomic Structure of Matter (CSSM),  
 Department of Physics, University of Adelaide 5005, Australia*

We examine how dynamical fermions affect both the UV and infrared structure of the QCD vacuum. We consider large  $28^3 \times 96$  lattices from the MILC collaboration, using a gluonic definition of the topological charge density, founded on a new over-improved stout-link smearing algorithm. The algorithm reproduces established results from the overlap formalism and is designed to preserve nontrivial topological objects including instantons. At short distances we focus on the topological charge correlator,  $\langle q(x)q(0) \rangle$ , where negative values at small  $x$  reveal a sign-alternating layered structure to the topological-charge density of the QCD vacuum. We find that the magnitudes of the negative dip in the  $\langle q(x)q(0) \rangle$  correlator and the positive  $\langle q(0)^2 \rangle$  contact term are both increased with the introduction of dynamical fermion degrees of freedom. This is in accord with expectations based on charge renormalization and the vanishing of the topological susceptibility in the chiral limit. At large distances we examine the extent to which instanton-like objects are found on the lattice, and how their distributions vary between quenched and dynamical gauge fields. We show that dynamical gauge fields contain more instanton-like objects with an average size greater than in the quenched vacuum. Finally, we directly visualize the topological charge density in order to investigate the effects of dynamical sea-quark degrees of freedom on topology.

PACS numbers: 12.38.Gc 11.15.Ha 12.38.Aw

## I. INTRODUCTION

The study of QCD vacuum structure is one area of research where lattice simulations provide access to otherwise unaccessible information. By generating typical vacuum gauge field configurations we are able to directly investigate their complex structure. Further, by varying the simulation parameters we can assess how different physical phenomena contribute to the structure of the vacuum. In particular, we are able to examine the effect of dynamical sea-quarks on the QCD vacuum.

A study of QCD vacuum structure at different scales usually requires the use of a filtering procedure. By removing the short-range UV fluctuations, one can probe the long-distance structural features of the vacuum. Typical UV filtering methods include cooling [1, 2, 3], APE [4, 5], and improved APE smearing [6], HYP smearing [7] and more recently, stout-link smearing [8] and LOG smearing [9]. More recently, the truncation of a spectral representation of operators using eigenmodes of the Overlap Dirac operator has been explored as a method to remove UV fluctuations [10, 11, 12, 13].

Instantons are believed to be an essential component of the long-distance physics of the QCD vacuum. The problem with most cooling and smearing algorithms is that they destroy the instantons in the vacuum. In particular, standard EXP, or stout-link, smearing suffers from this problem. In order to overcome this we employ a form of over-improved stout-link smearing [14, 15], described briefly in Sec. II.

One facet of recent topological studies of vacuum structure is the topological charge density correlator, or Euclidean 2-point correlation function

$$\langle qq \rangle \equiv \langle q(x)q(0) \rangle, \quad (1)$$

which is the integrand of the topological susceptibility

$$\chi \equiv \frac{\langle Q^2 \rangle}{V} = \int d^4x \langle q(x)q(0) \rangle, \quad (2)$$

where  $V$  is the 4-volume.

In Sec. III, we examine the shapes of the  $\langle qq \rangle$  correlator, using both over-improved stout-link smearing and 3-loop,  $\mathcal{O}(a^4)$  improved cooling. We use the gluonic definition of the topological charge density

$$q(x) = \frac{g^2}{32\pi^2} \epsilon_{\mu\nu\rho\sigma} \text{Tr}[F_{\mu\nu}(x)F_{\rho\sigma}(x)], \quad (3)$$

where

$$Q = \sum_x q(x), \quad (4)$$

and  $F_{\mu\nu}(x)$  is a 3-loop improved field strength tensor [16]. Of particular interest is the extent to which a purely gluonic definition of the topological charge density can reveal a negative  $\langle qq \rangle$  correlator. We then proceed to investigate how the correlator is affected by the inclusion of dynamical sea-quarks.

In Sec. IV we probe the infrared structure of the full dynamical QCD vacuum. We examine the extent to which instantons are found in the QCD vacuum and how the extra dynamical fermion degrees of freedom affect their distribution throughout the vacuum.

Finally, in Sec. V we directly visualize the topological charge density in order to investigate the effects of dynamical sea-quark degrees of freedom on topology. Conclusions are summarized in Sec. VI.

## II. OVER-IMPROVED STOUT-LINK SMEARING

Extended smoothing on any QCD gauge field will reveal the presence of smooth topological objects that are approximations to the classical Euclidean instanton solution. A single instanton has the gauge potential [17]

$$A_\mu(x) = \frac{x^2}{x^2 + \rho_{\text{inst}}^2} \left( \frac{i}{g} \right) \partial_\mu(S) S^{-1}, \quad (5)$$

where

$$S \equiv \frac{x_4 \pm i \vec{x} \cdot \vec{\sigma}}{\sqrt{x^2}}, \quad (6)$$

for instantons and anti-instantons.

Due to their correlations with low-lying Dirac eigenmodes these locally self-dual instanton-like objects are of obvious physical interest. Unfortunately it is well realized that standard smoothing procedures will often destroy instantons in the gauge field.

For this investigation we have chosen to employ over-improved stout-link smearing [14], and will now present a brief summary of the algorithm. Complete details and an investigation of the algorithm's performance are provided in Ref. [14]. We also present results using 3-loop improved cooling [16], and defer the reader elsewhere [6, 16, 18, 19] for a discussion of highly improved actions.

Standard stout-link smearing is closely related to the Wilson action

$$S_W(x) = \beta \sum_{\substack{\nu \\ \mu \neq \nu}} \frac{1}{3} \text{Re} \text{tr} [1 - U_\mu(x) \Sigma_{\mu\nu}(x)], \quad (7)$$

where

$$\begin{aligned} \Sigma_{\mu\nu}(x) &= U_\nu(x + \hat{\mu}) U_\mu^\dagger(x + \hat{\nu}) U_\nu^\dagger(x) \\ &+ U_\nu^\dagger(x + \hat{\mu} - \hat{\nu}) U_\mu^\dagger(x - \hat{\nu}) U_\nu(x - \hat{\nu}), \end{aligned} \quad (8)$$

to calculate the nearest neighbor contributions. However, it is possible to use any reasonable combination of links connected to the original link  $U_\mu(x)$ . We can analyze the effect of the Wilson action on an instanton by substituting the instanton solution into the Taylor expansion of  $S_W(x)$  [14, 20]

$$S_W^{\text{inst}} = \frac{8\pi^2}{g^2} \left[ 1 - \frac{1}{5} \left( \frac{a}{\rho_{\text{inst}}} \right)^2 - \frac{1}{70} \left( \frac{a}{\rho_{\text{inst}}} \right)^4 \right]. \quad (9)$$

If one plots this expression as a function of the instanton size  $\rho_{\text{inst}}$  one sees that the slope of the action is necessarily always positive. Denoting the action associated with a single classical instanton as  $S_0$ , we note that the ideal action for preserving instantons in the gauge fields would have a flat curve at  $S/S_0 = 1$ , as in the continuum.

In order to tame the lattice discretisation errors, improved actions have been developed, such as the Symanzik [21]  $O(a^2)$ -improved action

$$\begin{aligned} S_S &= \beta \sum_x \sum_{\mu > \nu} \left[ \frac{5}{3} (1 - P_{\mu\nu}(x)) \right. \\ &\quad \left. - \frac{1}{12} ((1 - R_{\mu\nu}(x)) + (1 - R_{\nu\mu}(x))) \right], \end{aligned} \quad (10)$$

where we have  $R_{\mu\nu}$  and  $R_{\nu\mu}$  to denote the different possible orientations of the rectangular loop, and  $P_{\mu\nu}$  denotes the plaquette.

We modify this action, following Perez *et al.* [20], by the inclusion of a new  $\epsilon$  parameter

$$\begin{aligned} S(\epsilon) &= \beta \sum_x \sum_{\mu > \nu} \left[ \frac{5 - 2\epsilon}{3} (1 - P_{\mu\nu}(x)) \right. \\ &\quad \left. - \frac{1 - \epsilon}{12} ((1 - R_{\mu\nu}(x)) + (1 - R_{\nu\mu}(x))) \right], \end{aligned} \quad (11)$$

where for  $\epsilon = 1$  we have the standard Wilson action, and for  $\epsilon = 0$  we have the Symanzik improved action. So by varying  $\epsilon$  between 0 and 1 we can effectively select how much improvement is included.

Alternatively we can set  $\epsilon < 0$  and over-improve the action. The advantage of a negative  $\epsilon$  value is that the leading order errors become positive upon substitution of the instanton solution

$$S^{\text{inst}}(\epsilon) = \frac{8\pi^2}{g^2} \left[ 1 - \frac{\epsilon}{5} \left( \frac{a}{\rho_{\text{inst}}} \right)^2 + \frac{14\epsilon - 17}{210} \left( \frac{a}{\rho_{\text{inst}}} \right)^4 \right]. \quad (12)$$

The curve of  $S/S_0$  is similarly affected. One sees that for a value of  $\epsilon = -0.25$  the curve is mostly flat and will preserve instantons objects on the lattice with size  $\rho_{\text{inst}}/a > 1.5$  [14].

Standard stout-link smearing, using an isotropic smearing parameter  $\rho_{\text{sm}}$ , involves a simultaneous update of all links on the lattice. Each link is replaced by a smeared link  $\tilde{U}_\mu(x)$

$$\tilde{U}_\mu(x) = \exp(iQ_\mu(x)) U_\mu(x), \quad (13)$$

where

$$\begin{aligned} Q_\mu(x) &= \frac{i}{2} (\Omega_\mu^\dagger(x) - \Omega_\mu(x)) \\ &- \frac{i}{6} \text{Tr}(\Omega_\mu^\dagger(x) - \Omega_\mu(x)), \end{aligned} \quad (14)$$

with

$$\Omega_\mu(x) = \rho_{\text{sm}} \sum \{1 \times 1 \text{ loops involving } U_\mu(x)\}. \quad (15)$$

The over-improvement parameter  $\epsilon$  is introduced into the smearing process by replacing the combination of links in

$\Omega_\mu(x)$  with

$$\Omega_\mu(x) = \rho_{\text{sm}} \sum \left\{ \frac{5-2\epsilon}{3} (1 \times 1 \text{ loops involving } U_\mu(x)) - \frac{1-\epsilon}{12} (1 \times 2 + 2 \times 1 \text{ loops involving } U_\mu(x)) \right\}. \quad (16)$$

Note that both forward and backward horizontally orientated rectangles are included in the  $2 \times 1$  loops, such that  $\Omega_\mu(x)$  resembles the local action. With this extended link path, we take  $\rho_{\text{sm}} = 0.06$ , smaller than the standard value of 0.1.

### III. TOPOLOGICAL CHARGE DENSITY CORRELATOR

#### A. Quenched QCD

The Euclidean 2-point correlation function for the topological charge  $q(x)$

$$\langle qq \rangle \equiv \langle q(x)q(0) \rangle, \quad (17)$$

also known as the topological charge density correlator, is negative for any  $x > 0$  [22, 23]. This follows simply from reflection positivity [24]. Given that the correlator must have a positive contact term  $\langle q^2(0) \rangle_x$ , the correlator necessarily has the form

$$\langle q(x)q(0) \rangle = A\delta(x) - f(x), \quad (18)$$

where  $f(x)$  is positive for all  $x$ .

Recent studies [10, 24] of vacuum structure using the overlap defined topological charge density have demonstrated the negativity of the topological charge density correlator in lattice simulations. The negative behavior of the  $\langle qq \rangle$  correlator suggests a sign-alternating layered structure to the topological charge density of the topological charge density correlator.

Hasenfratz [25] has also examined the shape of the 2-point correlator using APE smearing. For APE smearing the magnitude of the negative dip was far less than the current overlap results [10, 24]. We now attempt to obtain a negative  $\langle qq \rangle$  correlator similar to the overlap results using the new over-improved stout-link smearing algorithm and 3-loop improved gluonic operators for the action and topological charge densities [16]. In order to more closely compare with the overlap results we use quenched gauge fields for the initial calculation.

The gauge fields were generated by the MILC collaboration [26, 27] using a Tadpole and Symanzik improved gauge action with  $1 \times 1 + 1 \times 2 + 1 \times 1 \times 1$  terms in the quenched case and an Asqtad staggered dynamical fermion action for the  $2+1$  flavors of dynamical quarks. The lattice spacing for all three types of gauge fields is  $a = 0.09$  fm. For the specifics of how the gauge fields

TABLE I: The gauge fields used in this study. The lattices were generated by the MILC collaboration [26, 27]

Size	$\beta$	$a$	Bare Quark Masses
$28^3 \times 96$	8.40	0.086 fm	$\infty$
$28^3 \times 96$	7.09	0.086 fm	14.0 MeV, 67.8 MeV
$28^3 \times 96$	7.11	0.086 fm	27.1 MeV, 67.8 MeV

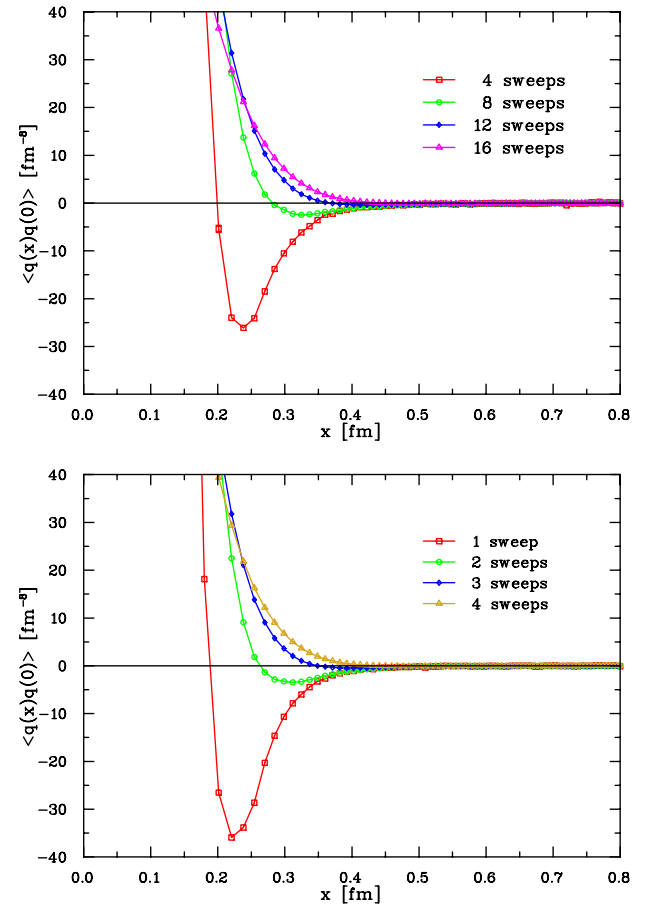


FIG. 1: The  $\langle qq \rangle$  correlator for a variable number of smoothing sweeps calculated on the quenched gauge fields. The top graph shows the  $\langle qq \rangle$  correlator for over-improved stout-link smearing smearing, and the lower graph for 3-loop improved cooling. Using four sweeps of smearing and one sweep of cooling it is possible to obtain a correlator similar to the recent overlap results [10, 24]. As more UV fluctuations are removed in successive smoothing iterations the correlator flattens off. Errors were calculated using the jackknife procedure but are too small to see.

were generated see Refs. [26, 27]. Simulation parameters are summarized in Table I.

We begin by investigating how the shape of the correlator changes as a function of the number of smearing sweeps. The results of our calculations are presented in Fig. 1. We see that for a small number of sweeps it is possible to generate a negative correlator, but that the negative behavior is largely suppressed after about

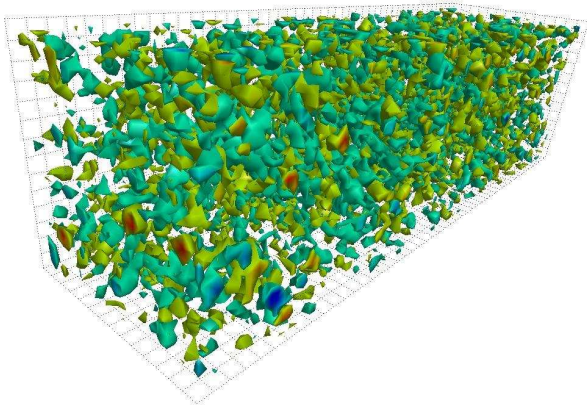


FIG. 2: The topological charge density of a quenched gauge field after four sweeps of smearing. Note the sign-alternating structure in the charge density.

10 sweeps and absent after around 40 sweeps.

The curves also have a positive core whose minimal size is limited by the lattice spacing and the combination of loops in the smoothing procedure. As more of the short-distance UV fluctuations are removed by the smoothing algorithm there is a dampening effect on the topological correlator.

One sweep of highly improved cooling gives a  $\langle qq \rangle$  correlator of similar proportions to the overlap defined correlator [10, 24], whilst for over-improved smearing, four sweeps reveals a similar curve. A quantitative comparison of the overlap correlator is performed in Ref. [12]. The topological charge density of a quenched field after 4 sweeps of smearing is presented in Fig. 2. There is considerable structure within the gauge field. A sign-alternating structure in the topological charge density is also apparent.

## B. QCD with Dynamical Fermions

We now investigate the effects of dynamical sea-quark degrees of freedom on topology. In quenched QCD the Witten-Veneziano [28, 29] formula gives a relation between the topological susceptibility and the mass of the  $\eta'$  meson [23]

$$\chi^{qu} = \frac{m_{\eta'}^2 F_\pi^2}{2N_f}. \quad (19)$$

However, in the full dynamical case the topological susceptibility should vanish in the chiral limit [23, 30]

$$\chi^{dyn} = \frac{f_\pi^2 m_\pi^2}{2N_f} + \mathcal{O}(m_\pi^4). \quad (20)$$

Of course, a vanishing topological susceptibility puts no restraints on how the function  $\langle q(x)q(0) \rangle$  should change with the addition of dynamical sea-quarks, it only requires that the integral of Eq. (2) vanish.

Including dynamical sea-quarks in the QCD action renormalizes the coupling constant. In order to maintain the same lattice spacing across quenched and dynamical gauge fields, one finds that the coupling parameter,  $g$ , must increase and hence  $\beta \sim 1/g^2$  must be smaller for the dynamical fields. In the QCD action formulated in Euclidean space,  $\beta$  appears as a factor governing the width of the probability distribution. When generating gauge fields, smaller  $\beta$  values permit greater fluctuations in the gauge links. The increased fluctuations can give rise to non-trivial field fluctuations, which will reveal itself in lattice simulations through a greater mean-square density  $\langle q^2(0) \rangle_x$ .

Given that in the chiral limit  $\chi^{dyn} = 0$ , it follows that an increasing mean-square density  $\langle q^2(0) \rangle_x$  must be compensated for by a stronger negative dip in the  $\langle qq \rangle$  correlator. The  $\langle qq \rangle$  correlator for the quenched ensemble and the two dynamical ensembles is shown in Fig. 3. These correlators were generated using four sweeps of over-improved stout-link smearing. We see that the contact term  $\langle q^2(0) \rangle_x$  is larger and the magnitude of the negative dip has also increased. These effects are stronger for lighter quark masses. This is of course expected because smaller quark masses require smaller  $\beta$  values. The exact values of the positive contact term are; quenched =  $2924 \pm 4 \text{ fm}^{-8}$ , heavy =  $5251 \pm 12 \text{ fm}^{-8}$ , light =  $5432 \pm 8 \text{ fm}^{-8}$

Hasenfratz [25] also observed an increase in the negative contribution to  $\chi$  with the addition of fermion loops. However, their correlators also show a decrease in the mean square density, which is in contrast to our results. This may be explained through the use of a standard smoothing algorithm, which is renowned for destroying topological objects in the gauge field.

## IV. INSTANTON-LIKE OBJECTS

### A. Profile Versus Charge Density

Understanding the nature of instanton-like objects in the QCD vacuum continues to be an active area of investigation. Considerable UV filtering reveals the presence of long-distance topological structures in the QCD vacuum. These topological objects are only approximations to the classical instanton solution, but are commonly referred to as instantons. The amount of smoothing usually applied in order to observe these instanton-like objects is far greater than the four sweeps of over-improved stout-link smearing that we used in the calculation of the  $\langle qq \rangle$  correlator.

We now analyze the similarity of the topological objects in the QCD vacuum to the classical instanton solution. Using over-improved stout-link smearing we are able to extract both the action and charge densities of our gauge fields. Starting with the action density we locate the positions of all local maxima in the field. The local maxima are identified by finding a point at the cen-

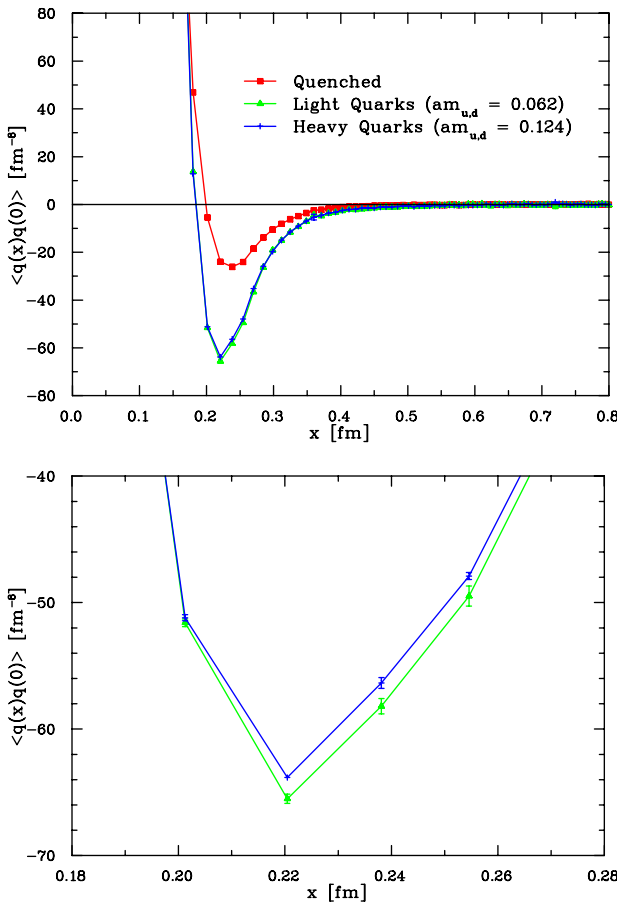


FIG. 3: A comparison of the  $\langle qq \rangle$  correlator for quenched and dynamical gauge fields. The smaller  $\beta$  values used for the dynamical fields result in greater field fluctuations that are visible through an increase in the magnitude of the negative dip. Although not shown, the contact term  $\langle q^2(0) \rangle_x$  has also increased and values are given in the text. The lower graph displays the same data as the upper graph, focusing on the negative dip for the dynamical fields. The magnitude of the dip is greater for the lighter quark mass.

ter of a  $3^4$  hypercube whose action density exceeds that of the neighboring 80 points of the hypercube.

Taking each maxima to be the approximate center of a possible instanton-like object we fit the classical instanton action density

$$S_0(x) = \xi \frac{6}{\pi^2} \frac{\rho_{\text{inst}}^4}{((x - x_0)^2 + \rho_{\text{inst}}^2)^4}. \quad (21)$$

to the measured action density. An arbitrary scale factor,  $\xi$ , is included to allow the *shape* of the action density to determine the size,  $\rho_{\text{inst}}$ . We fit the six parameters,  $x_0$ ,  $\xi$  and  $\rho_{\text{inst}}$  by fitting Eq. (21) to the action density of the aforementioned  $3^4$  hypercube.

From  $\rho_{\text{inst}}$ , one can infer the topological charge to be observed at the center of the distribution  $q(x_0)$  if it truly

is an instanton

$$q(x_0) = Q \frac{6}{\pi^2 \rho_{\text{inst}}^4}. \quad (22)$$

Here  $Q = \pm 1$  for an instanton/anti-instanton. This can then be compared with the topological charge measured directly from the charge density observed on the lattice.

A calculation on the ensemble of quenched gauge fields is presented in Fig. 4. Each cross represents a peak in the action density. If the peak were to exactly represent an instanton it would lie on the theoretical curve of Eq. (22). For a small number of sweeps we see that the peaks in the action density do not correspond well to instantons. It is only after extensive smearing has been applied that the objects start to approximate instantons.

After 40 sweeps of over-improved stout-link smearing we have a large number of maxima in the vacuum which appear to be good approximations to the classical instanton solution, at least within the  $3^4$  hypercube used to determine the “instanton” size.

While the core shape and density approximate an instanton, we now assess how similar the remainder of the object is to a classical instanton. To do so, we consider all points within a distance  $r$  measured relative to the instanton size  $\rho_{\text{inst}}$  and examine the extent to which the points within this distance have the same sign topological-charge density as observed at the center,  $q(x_0)$ . If the detected object is a good approximation to a classical instanton then all these points should have the same charge as  $q(x_0)$ .

In Fig. 5 we show the percentage of points that are within a relative distance  $r/\rho_{\text{inst}}$  of  $x_0$  that have the same sign as  $x_0$ . For small  $r/\rho_{\text{inst}}$  the percentage of sign-coherent points is close to 100, however it falls off rapidly as  $r$  approaches the characteristic size  $\rho_{\text{inst}}$ . This suggests that although the object is representative of an instanton at its center, the tails of the objects are distorted by vacuum fluctuations. What is remarkable is that at the characteristic size of the “instanton,” merely  $2/3$  of the points are sign coherent, suggesting that the objects revealed after 40 sweeps of smearing are good approximations of classical instantons only at the core.

## B. Dynamical Fermions and Instanton Structure

Given the strong correlation between  $q(x_0)$  extracted from the action density after 40 sweeps of smearing and that given by the classical solution (22) we can now compare “instanton” distributions between quenched and dynamical QCD.

We examine the variation in instanton size between the different gauge fields. A histogram of  $\rho_{\text{inst}}$  is shown in Fig. 6. Compared to the quenched ensemble, the dynamical gauge fields show an increase in average instanton size and also in the total number of instantons. A similar comparison was carried out in Ref. [31] where it was argued that the instanton distributions were the

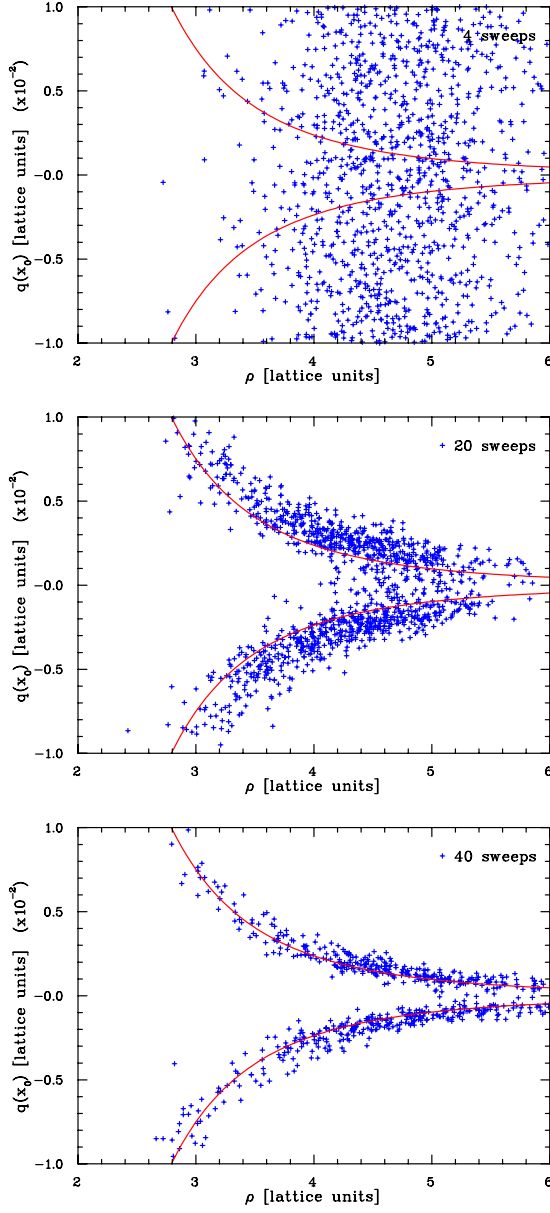


FIG. 4: A comparison of the charge at the center of the instanton-like objects  $q(x_0)$  observed on the lattice versus their size  $\rho_{\text{inst}}$  obtained via Eq. (21) for three different levels of over-improved stout-link smearing. From top to bottom we apply 4 sweeps, 20 sweeps and 40 sweeps of smearing. Each cross represents a local maxima in the action density of the gauge field. After 40 sweeps most points lie close to the classical curve.

same between quenched and dynamical gauge fields, however the results of that study were limited by statistical fluctuations.

It is often argued that the increased density of instanton-like objects on the lattice can be explained through an instanton/anti-instanton attraction occurring due to the presence of the fermion determinant in the QCD weight factor [30]. Isolated instantons and anti-instantons give rise to zero modes of the Dirac operator.

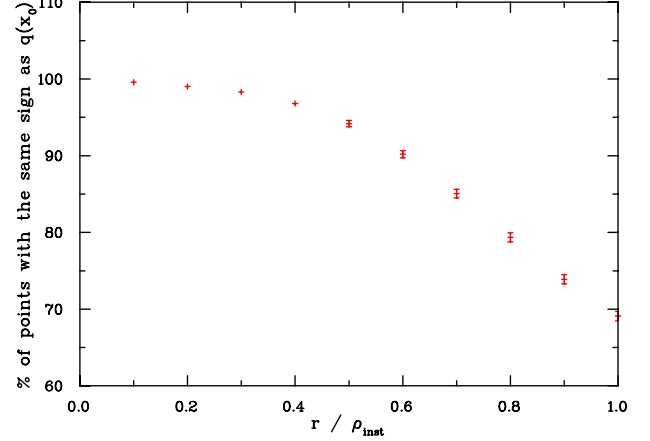


FIG. 5: The percentage of points that are sign coherent within a relative distance  $r/\rho_{\text{inst}}$  of each instanton-like objects' center  $x_0$  with size  $\rho_{\text{inst}}$ . For small  $r/\rho_{\text{inst}}$  the percentage of sign-coherent points is close to 100, however the sign-coherence falls off rapidly as  $r$  approaches the characteristic size  $\rho_{\text{inst}}$ .

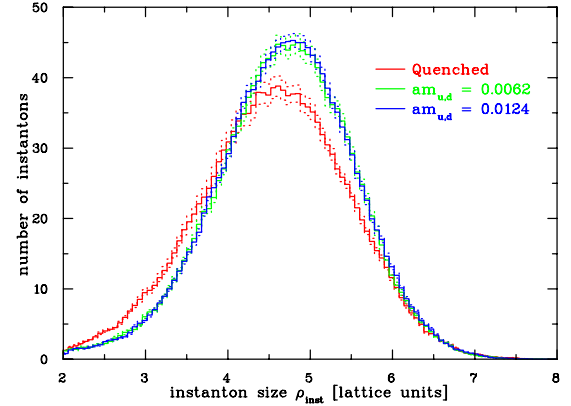


FIG. 6: A histogram of the instanton size  $\rho_{\text{inst}}$  in dynamical and quenched gauge fields. The dynamical fields show both an increase in the number of instantons detected and in average instanton size.

When generating dynamical gauge fields the selection of typical configurations is weighted by  $\det(\not{D} + m)e^{-S_g}$ . If an exact zero-mode of  $\not{D}$  were to exist on the lattice then the determinant would approach 0 in the chiral limit and it would be highly improbable that the configuration would be selected. Thus, isolated instantons will not exist in the light quark mass gauge fields and hence all instanton-like objects will be closer in these fields. This naturally leads one to expect that there will be a greater number of instantons in the dynamical gauge fields. However, this does not account for the increased average size of the topological objects, which is an interesting result.

## V. TOPOLOGICAL CHARGE DENSITY

The effects of dynamical quarks are realized significantly in the calculation of the  $\langle qq \rangle$  correlator. The increased magnitude of the non-trivial topological charge field fluctuations that are permitted due to the inclusion of fermion loops should also be visible in direct visualizations of the topological charge density.

Using four sweeps of over-improved stout-link smearing, we consider the short-range structure of the topological charge density. In Fig. 7 we present the topological charge density for the quenched and two dynamical ensembles. The extra field fluctuations that are permitted due to the fermion determinant are clearly visible in the visualizations of the dynamical QCD vacuum.

In Fig. 8 we compare the structure of the vacuum after 40 sweeps of over-improved smearing. It is difficult to observe the increased density of instantons in these figures. This is because the charge density fluctuates over different time-slices and a single time-slice does not always portray an accurate representation of the vacuum.

## VI. CONCLUSION

By applying two different levels of smearing to the large-volume MILC gauge fields, we explored the effects of dynamical fermions on topology. The results agree with expectations. The addition of fermions into the QCD action at constant lattice spacing renormalizes the coupling constant such that the coupling parameter  $\beta$  becomes smaller. This permits greater field fluctuations and is manifest through an increased RMS density of

topologically non-trivial field fluctuations. This induces an increased negative dip in the topological charge density correlator and a larger contact term reflecting the RMS density of topological charge density. This effect increases as  $m_{u,d} \rightarrow 0$ .

The results reflect the suppression of zero-modes due to the inclusion of the  $\det(\not{D} + m)$  weight factor in the selection of typical gauge fields, resulting in a decrease in the number of isolated instanton-like objects. This causes instantons and anti-instantons to be “attracted” [30] and leads to an increase in the density of instanton-like objects in the dynamical gauge fields.

These results support the emerging picture of the vacuum as an alternating “sandwich” of opposite topological charge density. Beneath this oscillating short-range structure there exists a long-distance foundation of instanton-like objects that can be revealed through smoothing. The addition of dynamical fermions allows stronger field fluctuations and a higher frequency of sign-oscillations in the topological charge density. The density of instanton-like objects beneath these short-distance oscillations also increases, as does their average size.

### Acknowledgments

The authors thank Ernst-Michael Ilgenfritz and Waseem Kamleh for constructive and insightful discussions. We also thank the Australian Partnership for Advanced Computing (APAC) and the South Australian Partnership for Advanced Computing (SAPAC) for generous grants of supercomputer time which have enabled this project. This work is supported by the Australian Research Council.

- 
- [1] B. Berg, Phys. Lett. **B104**, 475 (1981).
  - [2] M. Teper, Phys. Lett. **B162**, 357 (1985).
  - [3] E.-M. Ilgenfritz, M. L. Laursen, G. Schierholz, M. Muller-Preussker, and H. Schiller, Nucl. Phys. **B268**, 693 (1986).
  - [4] M. Falcioni, M. L. Paciello, G. Parisi, and B. Taglienti, Nucl. Phys. **B251**, 624 (1985).
  - [5] M. Albanese et al. (APE), Phys. Lett. **B192**, 163 (1987).
  - [6] F. D. R. Bonnet, D. B. Leinweber, A. G. Williams, and J. M. Zanotti, Phys. Rev. **D65**, 114510 (2002), hep-lat/0106023.
  - [7] A. Hasenfratz and F. Knechtli, Phys. Rev. **D64**, 034504 (2001), hep-lat/0103029.
  - [8] C. Morningstar and M. J. Peardon, Phys. Rev. **D69**, 054501 (2004), hep-lat/0311018.
  - [9] S. Durr (2007), arXiv:0709.4110 [hep-lat].
  - [10] E. M. Ilgenfritz et al., Phys. Rev. **D76**, 034506 (2007), arXiv:0705.0018 [hep-lat].
  - [11] I. Horvath et al., Phys. Rev. **D67**, 011501 (2003), hep-lat/0203027.
  - [12] E.-M. Ilgenfritz, D. Leinweber, P. Moran, K. Koller, G. Schierholz, and V. Weinberg (2008), arXiv:0801.1725 [hep-lat].
  - [13] F. Bruckmann, PoS **LATTICE 2007**, 006 (2007), arXiv:0710.2788 [hep-lat].
  - [14] P. J. Moran and D. B. Leinweber (2008), arXiv:0801.1165 [hep-lat].
  - [15] P. J. Moran and D. B. Leinweber, PoS **LATTICE 2007**, 383 (2007), arXiv:0710.2380 [hep-lat].
  - [16] S. O. Bilson-Thompson, D. B. Leinweber, and A. G. Williams, Ann. Phys. **304**, 1 (2003), hep-lat/0203008.
  - [17] A. A. Belavin, A. M. Polyakov, A. S. Shvarts, and Y. S. Tyupkin, Phys. Lett. **B59**, 85 (1975).
  - [18] P. de Forcrand, M. Garcia Perez, and I.-O. Stamatescu, Nucl. Phys. Proc. Suppl. **47**, 777 (1996), hep-lat/9509064.
  - [19] S. O. Bilson-Thompson, F. D. R. Bonnet, D. B. Leinweber, and A. G. Williams, Nucl. Phys. Proc. Suppl. **109A**, 116 (2002), hep-lat/0112034.
  - [20] M. Garcia Perez, A. Gonzalez-Arroyo, J. Snippe, and P. van Baal, Nucl. Phys. **B413**, 535 (1994), hep-lat/9309009.
  - [21] K. Symanzik, Nucl. Phys. **B226**, 187 (1983).
  - [22] E. Seiler and I. O. Stamatescu (1987), mPI-PAE/PT.
  - [23] E. Seiler, Phys. Lett. **B525**, 355 (2002), hep-th/0111125.
  - [24] I. Horvath et al., Phys. Lett. **B617**, 49 (2005), hep-lat/0504005.

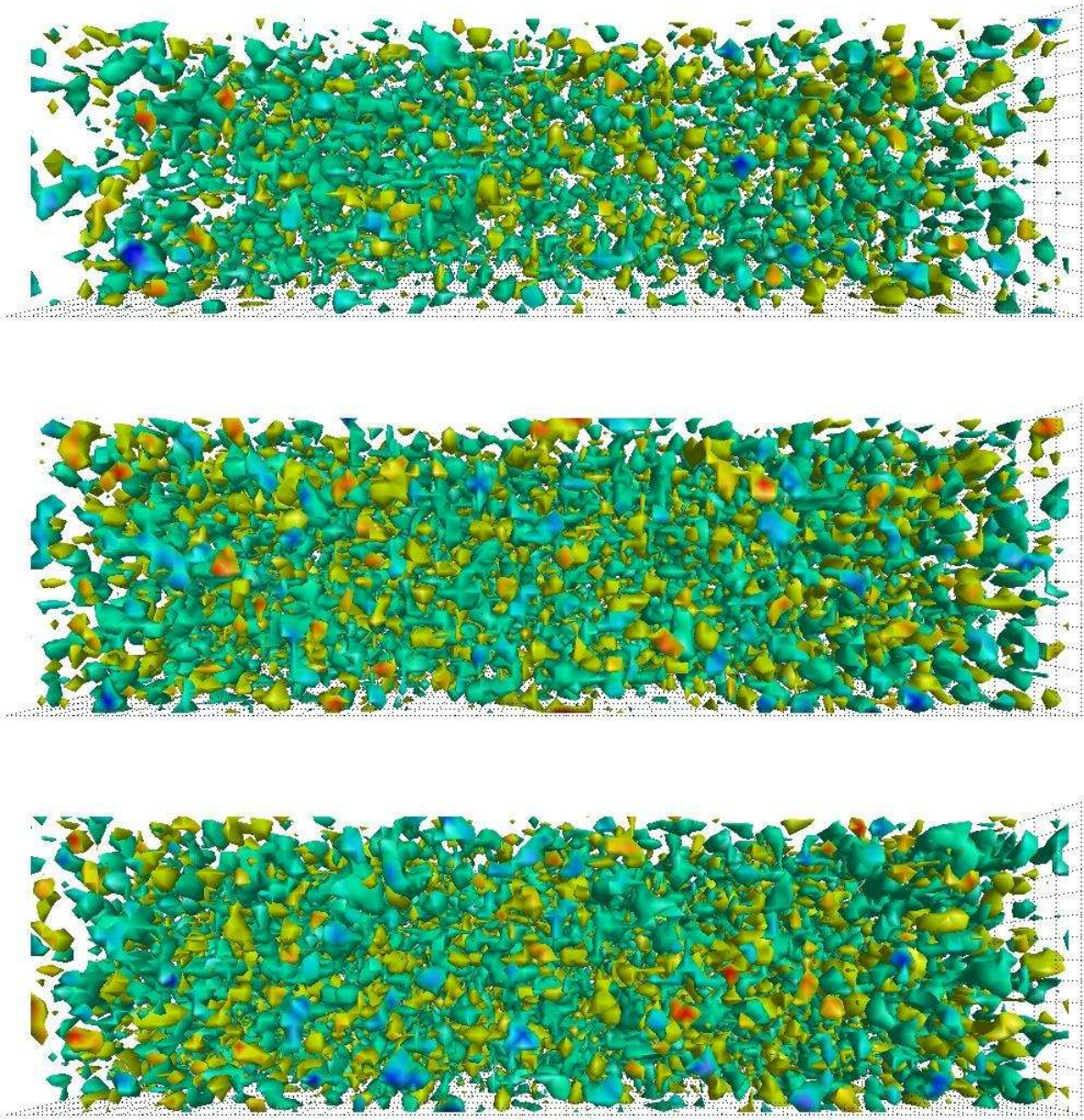


FIG. 7: The topological charge density for the quenched and dynamical ensembles, obtained after four sweeps of over-improved stout-link smearing. From top to bottom we plot a quenched field, the dynamical  $am_{u,d} = 0.0124$ ,  $am_s = 0.031$  field and the dynamical  $am_{u,d} = 0.0062$ ,  $am_s = 0.031$  field. The greater non-trivial field excitations that are permitted upon the introduction of light dynamical fermions are directly visible in the dynamical illustrations.

- [25] A. Hasenfratz, Phys. Lett. **B476**, 188 (2000), hep-lat/9912053.
- [26] C. Aubin et al., Phys. Rev. **D70**, 094505 (2004), hep-lat/0402030.
- [27] C. W. Bernard et al., Phys. Rev. **D64**, 054506 (2001), hep-lat/0104002.
- [28] E. Witten, Nucl. Phys. **B156**, 269 (1979).
- [29] G. Veneziano, Nucl. Phys. **B159**, 213 (1979).
- [30] A. Hart and M. Teper (UKQCD), Phys. Lett. **B523**, 280 (2001), hep-lat/0108006.
- [31] R. C. Brower, T. L. Ivanenko, J. W. Negele, and K. N. Orginos, Nucl. Phys. Proc. Suppl. **53**, 547 (1997), hep-lat/9608086.

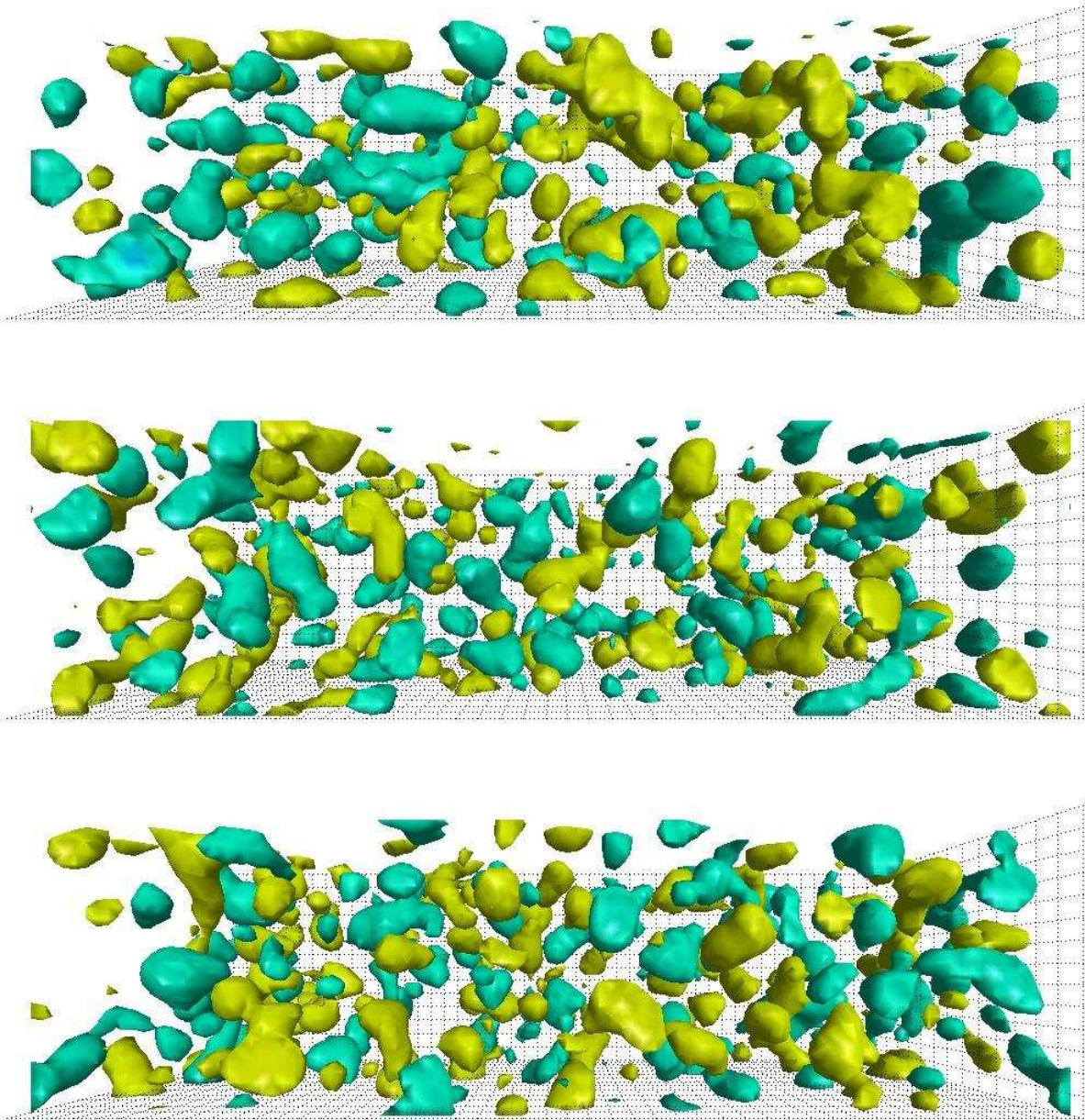


FIG. 8: The topological charge density for the quenched and dynamical ensembles, obtained after forty sweeps of over-improved stout-link smearing. From top to bottom we plot a quenched field, the dynamical  $am_{u,d} = 0.0124$ ,  $am_s = 0.031$  field and the dynamical  $am_{u,d} = 0.0062$ ,  $am_s = 0.031$  field. It is difficult to observe a noticeable difference in the size-distribution of the gauge field fluctuations when observing a single time-slice, but the sparseness of the quenched field is readily observed.